






ARTICLE

<https://doi.org/10.1038/s42005-019-0178-9>

OPEN

Room temperature continuous-wave excited biexciton emission in perovskite nanoplatelets via plasmonic nonlinear fano resonance

Jie Chen^{1,2,3}, Qing Zhang ^{3,4}, Jia Shi^{1,2}, Shuai Zhang^{1,2}, Wenna Du^{1,5}, Yang Mi¹, Qiuyu Shang^{3,4}, Pengchong Liu^{1,2}, Xinyu Sui^{1,2}, Xianxin Wu^{1,2}, Rui Wang¹, Bo Peng ⁶, Haizheng Zhong ⁷, Guichuan Xing⁸, Xiaohui Qiu^{1,2}, Tze Chien Sum ⁹ & Xinfeng Liu ^{1,2}

Biexcitons are a manifestation of many-body excitonic interactions, which are crucial for quantum information and computation in the construction of coherent combinations of quantum states. However, due to their small binding energy and low transition efficiency, most biexcitons in conventional semiconductors exist either at cryogenic temperatures or under femto-second pulse laser excitation. Herein, we demonstrated strong biexciton emissions from CsPbBr₃ nanoplatelets with continuous-wave excitation at room temperature by coupling them with a plasmonic nanogap. The exciton occupancy required to generate biexciton was reduced $\sim 10^6$ times in the Ag nanowire-Ag film nanogaps. The extremely large enhancement of biexciton emissions was driven by nonlinear Fano resonance between biexcitons and surface plasmon cavity modes. These results provide new pathways to develop high efficiency non-blinking single photon sources of biexciton (with spectral filter for biexciton), entangled light sources, and lasers based on biexciton states.

¹CAS Key Laboratory of Standardization and Measurement for Nanotechnology, CAS Center for Excellence in Nanoscience, National Center for Nanoscience and Technology, 100190 Beijing, China. ²University of Chinese Academy of Sciences, 100049 Beijing, China. ³Department of Materials Science and Engineering, College of Engineering, Peking University, 100871 Beijing, China. ⁴Research Center for Wide Band Semiconductor, Peking University, 100871 Beijing, China. ⁵Key Laboratory of Semiconductor Materials Science, Beijing Key Laboratory of Low Dimensional Semiconductor Materials and Devices, Institute of Semiconductors, Chinese Academy of Sciences, 100083 Beijing, China. ⁶National Engineering Research Center of Electromagnetic Radiation Control Materials and State Key Laboratory of Electronic Thin Films and Integrated Devices, University of Electronic Science and Technology of China, 610054 Chengdu, China. ⁷Beijing Key Laboratory of Nanophotonics and Ultrafine Optoelectronic Systems, School of Materials Science & Engineering, Beijing Institute of Technology, 100081 Beijing, China. ⁸Institute of Applied Physics and Materials Engineering, University of Macau, 999078 Macau, China. ⁹School of Physical & Mathematical Sciences, Nanyang Technological University, 21 Nanyang Link, Singapore 637371, Singapore. Correspondence and requests for materials should be addressed to Q.Z. (email: q_zhang@pku.edu.cn) or to T.C.S. (email: tzechien@ntu.edu.sg) or to X.L. (email: liuxf@nanoctr.cn)

Lead halide perovskites, with their outstanding carrier transport characteristics, high emission quantum yields, tunable bandgaps, and large absorption coefficients^{1–4}, have attracted considerable interest for applications across a range of technologies from solar energy conversion^{1,2,5} to light-emitting diodes (LEDs)⁶. Recently the energy conversion and LED efficiencies of lead halide perovskites reached 23.2% and 20.7%, respectively^{7,8}. In perovskites, electrons and holes are confined to inorganic $[\text{PbX}_6]^{4-}$ ($X = \text{Cl}, \text{Br}, \text{I}$) octahedral networks, which leads to enormous Coulomb interactions between electrons and holes and thereby, strong excitonic effects^{9,10}. In low-dimensional perovskite structures, i.e., nanocrystals (NCs) or nanoplatelets (NPLs), the electron–hole interactions are further enlarged as a result of the increased spatial overlap between electrons and holes. For instance, the exciton-binding energy of CsPbBr_3 bulk crystals is 40 meV¹¹, while the value increases to 120 meV in NCs¹². Furthermore, CsPbBr_3 perovskite NCs exhibit high photoluminescence (PL) quantum yield of $\sim 90\%$ ¹³. The large exciton-binding energy and high-quantum efficiencies of CsPbBr_3 perovskite NCs hold the key to the development of excitonic and quantum devices due to their stable excitons at room temperature. Furthermore, excitons in perovskite NCs may be coupled with free carriers, forming trions¹⁴. A trion can decay to a single electron (hole) by the emission of circularly polarized light, and it can achieve population inversion and laser action. The trion state shows a lower threshold compared with the neutral state, which requires a higher excited state to achieve optical gain. This is advantageous to realize low-threshold lasers¹⁵.

A biexciton is formed by two free excitons in condensed exciton systems¹⁶, two photon absorption¹⁷, or excitation from the single exciton state to the biexciton state. Biexcitons are of fundamental interest and practical importance for quantum information and computation due to their overwhelming advantage for constructing of coherent combinations of quantum states. The coherent control of biexcitons via their four physically distinguishable quantum states can be applied to basic quantum operations, i.e. two-bit physical quantum and conditional quantum logic gates^{18–20}. If fine structure splitting of the exciton state is smaller than the natural linewidth, the two indistinguishable radiative decay pathways of a biexciton can render a source of polarization entangled photon pairs. Furthermore, the nonlinear optical nature of the biexciton process can generate probabilistic number of entangled-photon pairs per excitation cycle²¹, which is similar to the standard entangled source parametric down conversion²² and four-wave mixing sources²³. Moreover, light sources based on biexciton may achieve no blinking and high saturation intensity^{24,25}. These intrinsic outstanding physical properties make biexciton interesting for inherent and coherent light sources including lasers, light emitting diodes, etc.^{26,27}. Till now, biexcitons have been realized in semiconductor heterostructures²⁸, NCs²⁶, and two-dimensional semiconductors^{16,29}, etc. Due to the small biexciton-binding energy and large Auger effect, biexcitonic effects have only been realized either under intense pumping by short pulsed lasers ($\sim \text{MW}/\text{cm}^2$) or in cryogenic conditions, which severely limits their practical applications. Resonant excitations can increase the probability of biexciton transition. For example, in quantum wells, biexciton emission was observed under a continuous wave (CW) excitation beam with a power of $\sim 70 \text{ mW}/\text{cm}^2$, but only below liquid helium temperature due to the small biexciton-binding energy^{30,31}. So far, CW excitation of biexciton at room temperature, which has fundamental practical significance is extremely challenging.

Plasmonic nanogap structures have been extensively explored in quantum electromagnetic dynamics due to their extraordinary capabilities for tailoring strong and weak light–matter interactions in the deep-subwavelength regime^{32–34}. In the last decade,

plasmonic nanogap have been widely used to enhance a variety of linear and nonlinear optical processes including emissions, hot carrier generation, Raman, high harmonic generation, etc.^{35–38}. Near a metal structure, the increasing local density of states in a plasmonic nanostructure can shorten the fluorescence lifetime and greatly suppress Auger recombination, even to the point where Auger recombination is negligible³⁹. When coupled to a metal structure, quantum dots (QDs) show super-Poissonian statistics of photon emissions, which is different from the behavior of QDs on quartz substrates that exhibit photon antibunching as single quantum emitters⁴⁰. In this case, QDs exhibit strong photon bunching which leads to multiexciton emissions⁴¹. This provides a way to achieve biexciton emissions with a significantly lower pump energy, which consequently highly suppresses the biexciton Auger recombination with decreasing pump density^{42–44}. The interactions between plasmons and QDs have been widely discussed^{41,45,46}. Surface plasmons are regarded as continuous energy states while quantum dot excitations are discrete energy levels. The coupling between continuous and discrete energy states leads to Fano effect^{47,48}. With increasing incident light intensity and enhanced coupling strength, the two-photon process will take the place of a single photon process which leads to nonlinear Fano effect^{45,49}.

In this work, we demonstrate strong biexciton emissions from CsPbBr_3 NPLs with continuous-wave excitation at room temperature, and the biexcitonic behavior is validated through experiments and simulations. By utilizing a Ag nanowire–Ag film nanogap structure, the exciton occupancy for biexciton emissions of CsPbBr_3 NPLs is reduced $\sim 10^6$ times. The extremely large enhancement of biexciton emissions is attributed to the nonlinear Fano resonance between the biexciton and surface plasmon cavity modes. Our experimental results provide new pathways to develop high efficiency non-blinking single photon sources with spectral filtering of biexciton emission, entangled light sources, lasers, and high-efficiency LED based on biexciton states.

Results

Schematic of biexciton and plasmonic structure. Figure 1a shows the energy level diagrams for the excitation and decay of a single exciton. The single exciton bright state can decay to the ground state by emitting one photon, while the dark state decays to the ground state mainly by nonradiative processes. Two states are coupled by a spin–flip process. For perovskite NCs, the dark state exhibit microsecond-order decay times with a lower energy⁵⁰. The dark state energy may be higher than that of the exciton due to the large Rashba spin-orbital effect⁵¹. Figure 1b shows the energy level diagrams of a biexciton. Biexciton is composed of two bright excitons and can decay to either of two single exciton states (bright state) accompanied by the emission of one photon³². The biexciton emission energy $\hbar\omega_{xx}$ is determined by the energy gap between the biexciton energy, E_{xx} and single exciton emission E_x via $\hbar\omega_{xx} = E_{xx} - E_x$. Therefore, when two excitons bind together to form one biexciton, the energy of the whole system decreases by $\Delta_{xx} = \hbar\omega_x - \hbar\omega_{xx}$, which is the so-called biexciton-binding energy. Figure 1c shows the two processes for the plasmon-enhanced biexciton state: NPLs absorb one electron–hole excitation to the exciton state (I) and then reach the biexciton state (II) by absorbing another one, while the electron–hole excitations in metal relax to the ground state. The plasmon excited by optical pumping decay by two following channels: (1) via transformation into photons and (2) via non-radiative decay into electron–hole excitations. The latter fall into two categories: intraband excitations and interband excitations⁵². As the dephasing time of perovskite is much longer than silver nanowire⁵³, electron–hole excitations in plasmonic cavity decay

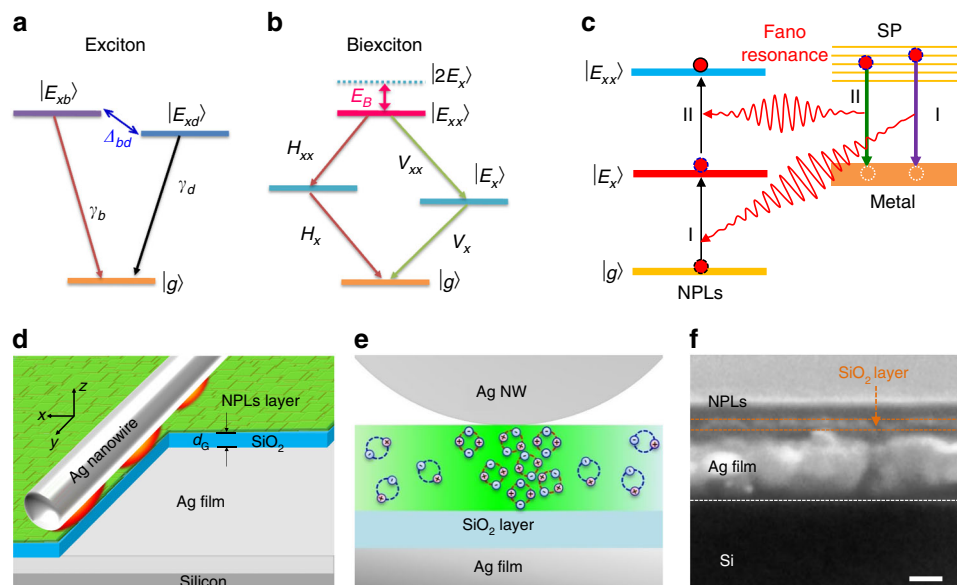


Fig. 1 Schematic of biexciton and formation process. **a** Schematic diagram of exciton and biexciton transitions. Exciton has a bright state which can arrive in the ground state by radiation or non-radiation transitions. The corresponding dark state coupled through a spin-flip process arrives in the ground state mainly by non-radiation transitions. The dark state energy may be higher than that of the exciton due to the large Rashba spin-orbital effect. **b** The biexciton levels are formed by a four-level system: biexciton level, two bright exciton levels, and ground state. The two bright exciton levels are separated by fine structure splitting. The biexciton decays through a cascade process of either emitting two horizontally or vertically polarized photons. **c** Schematic diagram of biexciton formation process with nonlinear Fano effect. Nanoplatelets (NPLs) absorb one electron-hole excitation to the exciton state (I) and then reach the biexciton state (II) by absorbing another one, while the electron-hole excitations in metal relax to the ground state. **d** Schematic view of the structure. The cavity is composed of a Ag nanowire and Ag substrate separated by a SiO₂ gap of 5 nm and perovskite nanoplatelets. **e** Schematic view of the exciton and biexciton in the cavity. The NPL is covered with 4-Methyl-1-acetoxycalix[6]arene molecular. **f** Cross-sectional scanning electron microscope (SEM) image of the sample. The scale bar is 20 nm

and perovskite NPLs obtain the energy. The resonant effect between the plasmonic cavity and the perovskite biexciton energy extensively promote excitation cross-section of biexciton, which leads to an increased biexciton transition. The electron-hole excitations in metallic material loses energy via electron-phonon coupling on a picosecond time scale⁵⁴. The Fano resonance can be set up within 10 fs which is much faster than electron-hole excitations decay time in plasmon⁵⁵. Our designed structure is shown in Fig. 1d, which is a sandwiched structure of silver (Ag) nanowire/NPLs/Ag film. A thin layer of SiO₂ and perovskite NPLs were coated onto Ag film step by step. SiO₂ was used to control the gap width d_G between the Ag nanowire and film and also prevent the perovskite NPLs from PL quenching nearby metal surface. To reduce the scattering and radiation losses in the plasmonic nanogap due to surface discontinuity, the growth condition of the SiO₂/Ag film was optimized with a surface roughness ~ 1.1 nm (Supplementary Note 1). Figure 1e shows the schematic of the biexcitons of CsPbBr₃ PLNs in the plasmonic nanogap. Perovskite NPLs (Supplementary Note 2) were deposited onto the SiO₂ layer by solution-processed spin-coating methods. To isolate the perovskite NPLs with Ag nanowire, the 4-Methyl-1-acetoxycalix[6]arene (4M1AC6, 0.5% in chlorobenzene) polymer film was spin-coated onto the CsPbBr₃ NPLs. The thickness of the perovskite NPL layer and polymer film was 13 nm, as measured by ellipsometry (Supplementary Note 3). A cross-section SEM image (Fig. 1f) shows that the perovskite NPL layer was uniform in scale of millimeters.

Crystal structure of perovskite NPLs. Transmission electron microscopy (TEM) images of the CsPbBr₃ NPLs are presented in Fig. 2a. The dispersed CsPbBr₃ NPLs had an average lateral size of 30 nm. HRTEM images of the CsPbBr₃ NPLs in Fig. 2b, combined with single photoluminescence (PL) peak in solution

(Supplementary Note 4), confirms that the CsPbBr₃ NPLs possessed good crystallinity. The Fourier transform diffraction spot is illustrated at the upper right corner, which shows the perovskite NPLs cubic crystal structure with a 5.92 Å lattice constant. X-ray diffraction (XRD) patterns within the 2θ range of 10–50° were recorded at room temperature and are shown in Fig. 2c. The XRD pattern of the CsPbBr₃ NPL show strong diffraction peaks, which were assigned to the pure cubic crystal structure¹³ consistent with the HRTEM Fourier transform diffraction spot. The thicknesses of the CsPbBr₃ NPLs are shown in Fig. 2d with the atomic force microscopy (AFM) image on SiO₂/Si substrate. A single CsPbBr₃ NPL was characterized in Fig. 2e with a height ~ 4 nm and a lateral size ~ 30 nm corresponding to the TEM lateral size shown in Fig. 2b. Thickness statistics of the CsPbBr₃ NPLs are shown in Fig. 2f with an average thickness ~ 3.8 nm and an exciton-binding energy of ~ 120 meV (Supplementary Note 5). Combined with the excitonic Bohr radius of 7 nm¹³, the NPLs exhibited a strong confinement in the z direction.

Cavity-coupled perovskite NPLs fluorescence. To probe the biexciton effect in perovskite NPLs, PL of the perovskite NPLs on and off the plasmonic nanogaps was performed with a CW laser (Fig. 3, wavelength: 405 nm; spot diameter: 2 μm). The PL spectrum far from the plasmonic nanogap (P1, blue line) was assigned to single exciton recombination of CsPbBr₃⁵⁶. It shows a single symmetric peak located at 500 nm, which corresponds to a free exciton when the excitation power P is 1.6 μW. In contrast, on the nanogap (P2, red line), a new peak arouse at 520 nm with an intensity much higher than that of single exciton emission. Although the nanowire is much smaller than the excitation spot diameter. Two obvious phenomena can be seen: (1) the strong biexciton emission is observed, which comes from the perovskite NPLs in the plasmonic cavity due to nonlinear Fano effect; (2) the

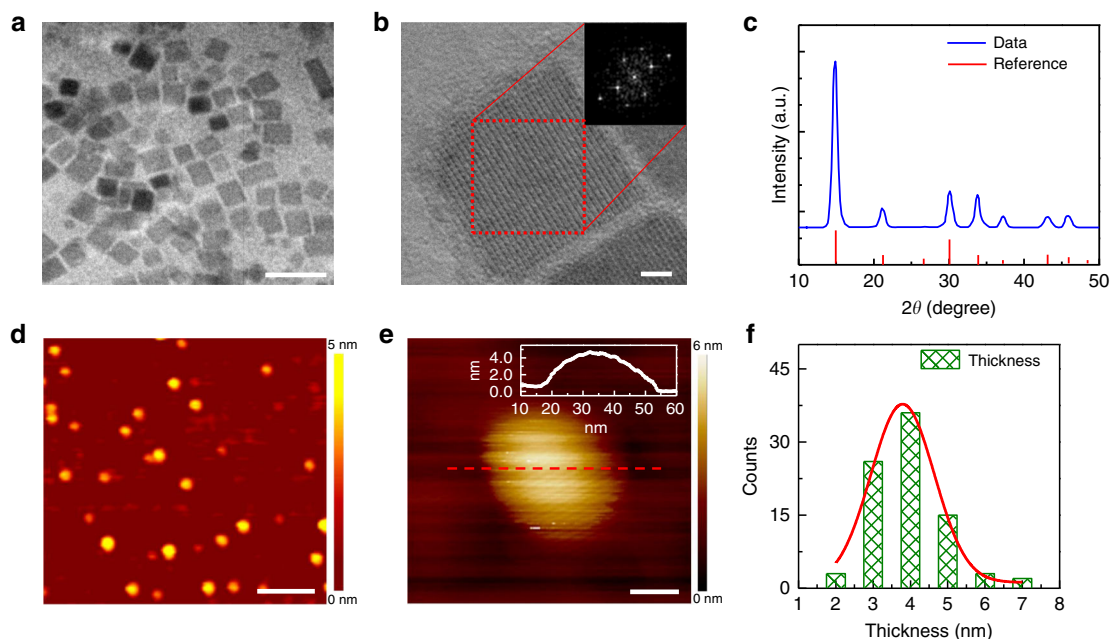


Fig. 2 Crystal structure of perovskite nanoplatelets (NPLs). **a** Transmission electron microscopy (TEM) image of CsPbBr₃ NPLs. The scale bar is 50 nm. **b** High-resolution transmission electron microscopy (HRTEM) images of CsPbBr₃ NPLs and the Fourier transform diffraction spot. The scale bar is 5 nm. **c** X-ray diffraction (XRD) pattern of CsPbBr₃ NPLs. **d** Atomic force microscope (AFM) image (500 nm × 500 nm) of CsPbBr₃ NPLs on SiO₂/Si substrate. The scale bar is 100 nm. **e** The single CsPbBr₃ NPL shown in **a** with a height ~4 nm and a lateral size ~30 nm corresponding to TEM size shown in **b**. The scale bar is 10 nm. **f** Thickness statistics of CsPbBr₃ NPLs which shows an average thickness ~3.8 nm

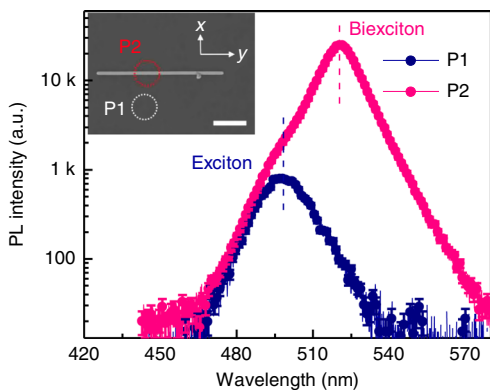


Fig. 3 Spectral characteristics of cavity-coupled perovskite nanoplatelets (NPLs) fluorescence. Perovskite NPL off-cavity fluorescence spectrum (P1) shows a single symmetric exciton peak at 500 nm, while in the on-cavity spectrum (P2), a biexciton peak at 520 nm under continuous wave radiation emerged. The binding energy of the biexciton is about 95 meV. The inset is an scanning electronic microscopy (SEM) image of a cavity (scale bar 1 μm), illustrating the location of the incident laser spot for the on-cavity (P2) and off-cavity (P1) measurements. The error bar corresponds to the standard deviation of the measurements

exciton emission signal on silver nanowire is about three times (Fig. 3) than that off nanowire, which is attributed to the perovskite NPLs in the plasmonic cavity area due to strong field enhancement. These results suggest that the plasmonic nanocavities yield a strong effect in the biexciton emission process (the corresponding linear coordinate PL spectrum is shown in Supplementary Note 6). The energy difference between the single exciton (500 nm, 2.480 eV) and new emission peak (520 nm, 2.385 eV) was ~95 meV, which is almost the same as the

biexciton-binding energy of CsPbBr₃ quantum dot reported previously (~100 meV)²⁷.

Power law of perovskite NPLs PL integral intensities. Under full thermal equilibrium conditions of the biexciton recombination process, the emission intensity of biexciton I_{bx} is proportional to the square of the single exciton emission intensity I_{ex} ^{57,58}. And biexciton lifetime is about half of single exciton lifetime. Excitation power-dependent PL and time-resolved PL (TRPL) spectroscopy were conducted to confirm the occurrence of biexciton. Figure 4a, b shows the power-dependent PL spectra on and off the Ag nanowire on the Ag film, respectively. Figure 4c shows the integrated emission intensity of exciton (I_{ex}) and biexciton (I_{bx}) as a function of the fluence intensity P . As the pumping power increased from 20 to 130 μW, the PL spectrum away from the plasmonic nanogap (Fig. 4a) showed one emission peak at 500 nm with the intensity I exhibiting a linear dependence on the pumping power P (Fig. 4c, purple), which is ascribed to single exciton recombination. However, on the plasmonic nanogap, a 520 nm peak due to biexciton emissions emerged, with the intensity I_{bx} growing more rapidly than that of the single exciton (Fig. 4b). Although the biexciton emission peak onset emerged when $P > 100$ mW/cm² (0.5 μW, ~20 μm) (Supplementary Note 7), we performed emission spectroscopy with $P > 500$ W/cm² (20 μW, ~2 μm) to lower the fitting error, when separating the power dependence of the biexciton emission from that of the single exciton emission. Figure 4c shows the integrated emission intensity of the exciton (I_{ex}) and biexciton (I_{bx}) as a function of the fluence intensity. The power dependence of the biexciton emissions could be described adequately by a superlinear function with a power law of $k = 1.83$. The power law of the biexciton (1.83) was about 1.91 times greater than that for the single exciton (0.96), strongly suggesting the occurrence of biexciton emissions.

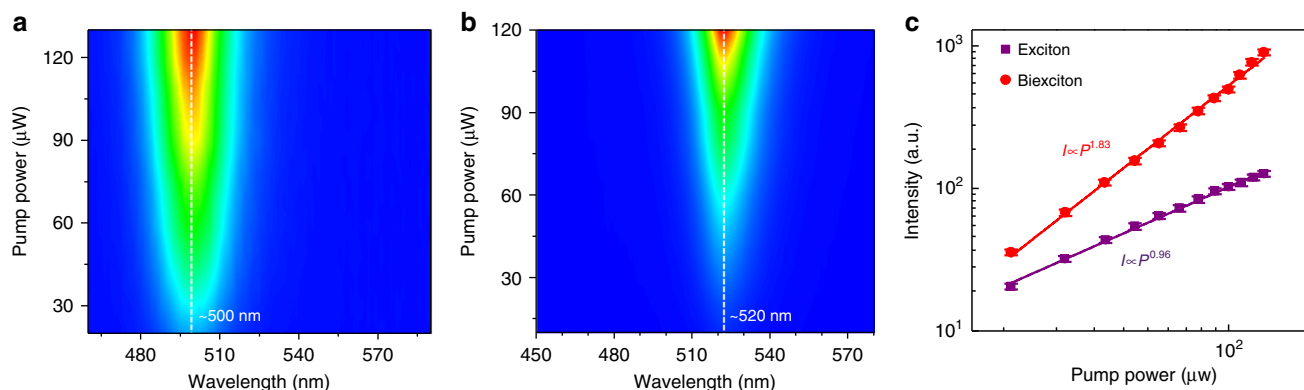


Fig. 4 Photoluminescence spectra and integral intensities of perovskite nanoplatelets (NPLs) for different pump fluences. **a** PL spectroscopy of the nanogap only showed exciton recombination peaks as the pumping power increased from 20 to 130 μW . The emission intensity is linear with pumping power (**c**, purple). **b** The biexciton emission peak of 520 nm at high excitation fluence. With increasing pumping power, the biexciton, however, grows much faster than that of single exciton. The same color map is used to make a clear comparison. **c** A log-log scale was adopted to plot the integrated emission intensity strength, I_p , as a function of the exciton emission strength P . The purple line is a power-law fit $I_p = P^{k_1}$, with a power-law constant $k_1 = 0.96$, while the red line $k_2 = 1.83$. The ratio $l = k_2/k_1$, has a value of 1.91. This provides strong evidence that **a** shows exciton luminescence while **b** shows biexciton fluorescence. The error bar corresponds to the standard deviation of the measurements

Lifetimes of excited states. Further, TRPL spectroscopy was conducted to probe the exciton and biexciton dynamics. Quantitatively under the condition of thermal equilibrium, the time evolution of the exciton and biexciton can be modeled with the transition function⁵⁹ $n_{\text{bx}} \sim n_{\text{bx}}^0 e^{-2t/\tau_{\text{ex}}}$, where exchange interactions between excitons with different spin are ignored. In other words, the biexciton decay rate is indeed about twice that of single exciton, as suggested in bulk semiconductor⁶⁰, QDs⁵⁹, quantum wells⁶¹, and 2D semiconductors⁶². Figure 5a, b show the TRPL spectra of the CsPbBr₃ NPLs on (a) and off (b) the plasmonic nanogap. To avoid any biexciton effects away from plasmonic nanogap under high pumping conditions, the excitation fluence of the femto-second pulsed laser was $\sim 0.1 \text{ nJ}/\text{cm}^2$, and thereby, the PL spectra showed only single exciton emission. The single exciton recombination curve could be well fit by a single exponential decay function with a time constant of $\tau_{\text{ex}} = 1170 \pm 10 \text{ ps}$. The TRPL spectroscopy of the biexciton emission was pumped with a power $\sim 70 \text{ nJ}/\text{cm}^2$ and could be well-fit by a single exponential decay curve, suggesting the emissions on the plasmonic nanogap were dominated by biexciton recombination. The lifetime of the biexciton $\tau_{\text{bx}} = 510 \pm 5 \text{ ps}$, was half of single the exciton lifetime ($1170 \pm 10 \text{ ps}$), which is consistent with the transition properties of the biexciton states as discussed above. Therefore, we can conclude that the 520 nm peak arising on plasmonic nanogap was due to biexciton recombination.

Fano effect of silver nanowire and perovskite NPLs. In the plasmonic nanogap, biexciton emission was observed when the pumping fluence exceeded $100 \text{ mW}/\text{cm}^2$ (Supplementary Note 7). The estimated exciton occupancy (N) $\sim 10^{-5}$ was much lower than 1, which indicates that the biexciton emission were not produced by exciton–exciton bounding in this nanogap region. However, the enhancement factor should be much larger than the local field enhancement factor (< 100 , Supplementary Note 8) in the plasmonic nanogap. This indicates that the enhanced biexciton emission was not mainly due to local field enhancement. Moreover, the Purcell effect of the NPLs was observed in the plasmon nanocavity and the factor is ~ 2.5 (Supplementary Note 9). However, it did not play an important role in biexciton formation process and can be negligible.

Biexciton forms mainly through the following three methods: (1) two photon absorption, (2) exciton–exciton bounding in

condensed exciton environment, and (3) resonant excitation from a single exciton. The first two pathways required intense pumping, which is not feasible under CW excitation conditions. To confirm that the plasmon mode affected the biexciton between the Ag nanowire and Ag film, the emission polarization behavior was measured. As shown in Fig. 6a, the biexciton emission was strongest when the excitation polarization direction was parallel to the long axis of the nanowires ($0^\circ, 180^\circ$) and weakest when the excitation polarization direction was perpendicular to the long axis ($90^\circ, 270^\circ$). However, the emission intensity of the perovskite NPLs away from the Ag nanowire was almost the same (Supplementary Note 10). The polarization resolved emission properties of the 520 nm peak suggests the modulation of the Ag nanowire’s plasmonic mode which is transverse magnetic mode. Moreover, an asymmetric peak appeared with a zero detuning position around the perovskite biexciton resonant energy, resulting from Fano interference between biexciton resonance excitation and background continuum states excitation of surface plasmon modes as shown in Fig. 6b. The scattering spectra were fitted with Fano-line profiles, $\sigma_{\text{sca}} = A [(q + \Omega)^2 + B] / (1 + \Omega^2)$, where q is the Fano parameter, $\Omega = 2(E - E_0)/\Gamma$, Γ is the resonant width and E_0 is the resonant energy, which is centered at the biexciton emission position⁶³. The fitted Fano factors were -0.25 and -0.2 , when the polarization was parallel and vertical to long axis of nanowire, respectively. The scattering lineshape was simulated by the finite-difference time-domain (FDTD) method, as shown in Fig. 6c. It is noticed that the nonlinear Fano resonance lineshape was only observed in the scattering spectra of the Ag nanowire–NPLs–Ag film system with strong biexciton emissions, which suggests that the exciton–plasmon energy transfer plays a vital role in the formation of biexciton. Plasmon resonant energy transfer can only occur when the plasmon peak overlaps with the biexciton states (Supplementary Note 11). Without energy transfer, the NPLs in the gap only show exciton emission (Supplementary Note 12). The nonlinear interaction witnessed as the Fano resonance contributed to the biexciton emission.

The nonlinear Fano resonance suffers from the distance of metal structure with NPLs and external field. With a gap of 13 nm and external field of $0.1 \text{ W}/\text{cm}^2$, the interaction can be viewed as linear interaction dominant, which can be seen as the threshold of biexciton emissions^{45,49}. Due to the large binding energy of the CsPbBr₃ NPLs, room temperature biexciton emissions off the

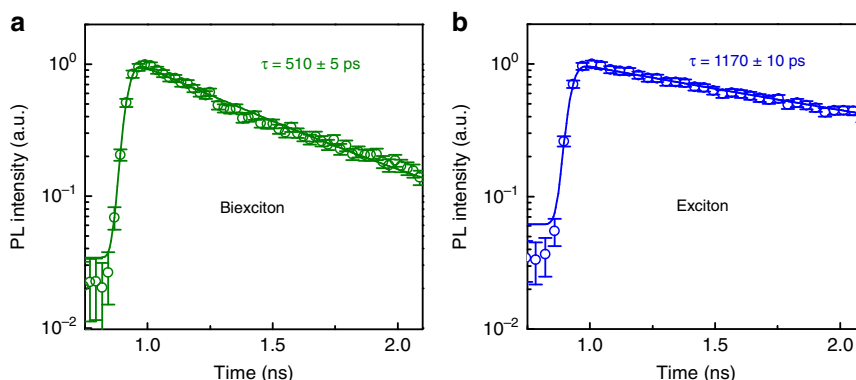


Fig. 5 Dynamics of excited states. **a** Time-resolved photoluminescence of biexciton which can be seen as a single decay process shows that the lifetime is $\tau_{bx} = 510 \pm 5$ ps. **b** Single index decay of exciton and fit with a lifetime of $\tau_{ex} = 1170 \pm 10$ ps represents the electron-hole recombination dominating the photoluminescence. The lifetime of the exciton is approximately twice that of the biexciton. Here, the extracted ratio ~ 2.29 is consistent with the theoretical result. The error bar corresponds to the standard deviation of the measurements

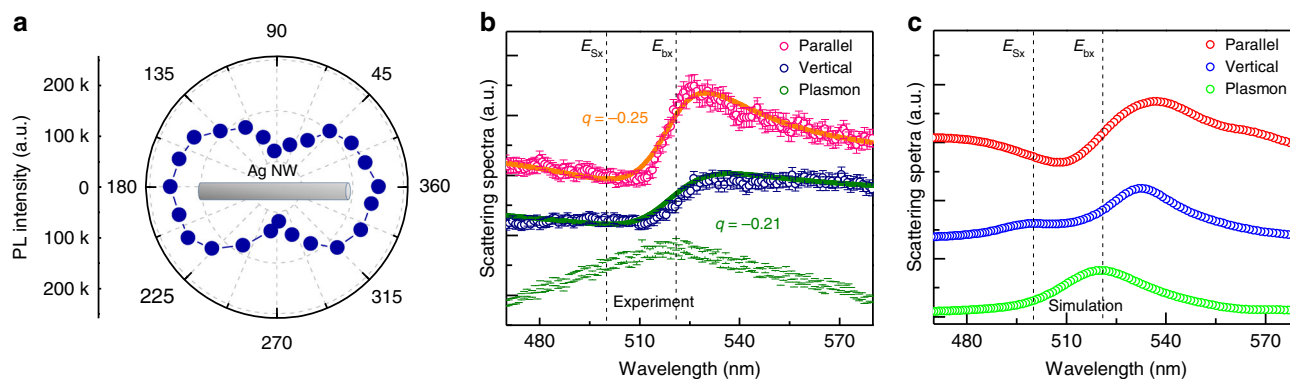


Fig. 6 Fano effect of silver nanowire and perovskite nanoplatelets (NPLs). **a** Polarization of the biexciton shows the biexciton is along the Ag nanowire. **b** Plasmon resonant spectra of the nanogap shows a single symmetrical peak shown as a green dotted line. The plasmonic nanogap with perovskite NPLs shows a symmetrical peak. Red and blue dotted lines show the scattering spectra with parallel and vertical polarizations, respectively. **c** Finite-difference time-domain (FDTD) simulation results of **b**. The error bar corresponds to the standard deviation of the measurements

nanogap could be excited only by fs laser pulse of amplifier (1 kHz, 80 fs) and the pumping fluence was on the magnitude of $\sim 10^{11}$ W/cm² with an estimated average NPL exciton occupancy $\langle N \rangle \sim 30$ (Supplementary Note 13). The threshold in our system was much higher than $\langle N \rangle \sim 1$, since a larger pump intensity leads to ionization⁶⁴ and a faster Auger recombination rate with a very rapid growth of the carrier density⁶⁵. To make sure the NPLs is not damaged, the increasing and decreasing power-dependent PL is measured (Supplementary Note 14). Moreover, the power-dependent PL is also pumped with fs laser pulses of oscillator (80 MHz, 100 fs), however, biexciton is not emerged until NPLs is damaged (Supplementary Note 15). Therefore, the exciton occupancy to generate biexciton in the plasmonic nanogap was reduced by $\sim 10^6$ times when comparing with fs laser pulse of amplifier.

Discussion

A resonant excitation process is proposed to explain the huge biexciton effect driven by surface plasmon cavity. As shown in Fig. 1b, since the single exciton–biexciton transition energy was nearly the surface plasmon energy, a nonlinear process with energies ω and ω' can be absorbed through resonant energy transfer from surface plasmons to NPLs, leading to the excitation of biexciton and annihilation of surface plasmons. The

interference of the two excitation processes results in the non-linear Fano resonance lineshape in the scattering spectra, where an asymmetric peak confirmed the process occurred. The surface plasmon-driven mechanism is similar to the biexciton generation by a resonant pump-probe in single carbon nanotube⁶⁶. The highly populated energy of plasmon was confirmed by zero detuning position of scattering spectra, which is almost overlapped with the biexciton transition energy. The resonance effect extensively promoted the excitation cross-section of biexciton from exciton states.

In conclusion, we found clear evidence for the presence of high-efficiency biexciton generation in perovskite NPLs in a metallic nanostructure under CW pumping at room temperature. The observation of the biexciton was a consequence of the clear emission spectra besides exciton with a binding energy ~ 95 meV, which was verified by the activation energy. The fluorescence power law and lifetime provided further evidence of the biexciton emission. Moreover, the nonlinear Fano effects were confirmed by measuring the scattering spectrum. By fitting the spectrum with Fano parameters and FDTD simulations, we are sure that this demonstration of the four-particle complex in plasmonic nanostructure will give rise to new interesting effects, such like quantum logic gates, Bose–Einstein condensation of exciton, source of polarization-entangled photons, single-photon source and high-efficiency LEDs.

Methods

Sample preparation. The SiO₂/silver substrate was made through magnetron sputtering with silver thickness of 50 nm and SiO₂ thickness of 5 nm on a SiO₂/Si substrate. CsPbBr₃ NPLs were spin-coated on the SiO₂/silver substrate at a speed of 3000 r/min. The 4-Methyl-1-acetoxycalix[6]arene (4M1AC6, 0.5% in chlorobenzene) was spin-coated on the CsPbBr₃ NPLs at a speed of 5000 r/min. After waiting for about 30 min to allow the 4M1AC6 to dry, silver nanowires were spin-coated in isopropyl alcohol at a speed 2000 r/min.

SEM and TEM measurements. The samples were forced apart after liquid nitrogen treatment. The SEM equipment was a Merlin-61-53 with a working distance of 4.3 mm and a voltage of 5 kV. The perovskite NPLs for the TEM measurement were dropped onto TEM grids. High-resolution transmission electron microscopy (HRTEM) was performed with an FEI Tecnai F20 operated with an acceleration voltage of 200 kV.

Time-resolved PL spectroscopy. For time-resolved PL measurements, the excitation pulses (wavelength 400 nm) were doubled frequencies of a Coherent Mira 900 (120 fs, 800 nm, 76 MHz) and filtered by a 655 short-pass filter to generate 400 nm light. The backscattered signal was collected using a time correlated single photon counting (TCSPC, SPC-150) which has an ultimate temporal resolution of ~40 ps. A 442 nm long-pass filter was placed before the optical fiber to filter out the residual 400 nm light.

PL measurements. The output from a 405 nm CW laser was circularly polarized by a quarter-wave plate, and focused on a sample by a microscope objective lens ($\times 100$, NA = 0.95, with spot size ~2 μ m). The PL signal was then back collected by the same lens, and filtered by a long-pass filter before entering a spectrometer (PI Acton 2500i with a liquid nitrogen-cooled charge coupled device—CCD camera). The low-temperature PL was measured when the sample was in the liquid nitrogen refrigeration cryogenic instrument.

FDTD simulation. The FDTD simulations of the silver nanowire and QDs were simulated using the Lorentz model⁶⁷. We modeled the CsPbBr₃ nanoplatelet layer using a dielectric function as a single Lorentzian function. The dielectric constant for bulk CsPbBr₃ is 3.8⁶⁸. The biexciton energy and plasmon resonant energy transfer were considered, while other high-order transitions were ignored. The biexciton linewidth was used as the transition linewidth. The metal dielectric function was treated as a Lorentz–Drude model.

Data availability

The data that support the findings of this study are available from the corresponding author upon reasonable request.

Received: 4 November 2018 Accepted: 23 May 2019

Published online: 12 July 2019

References

- Liu, M., Johnston, M. B. & Snaith, H. J. Efficient planar heterojunction perovskite solar cells by vapour deposition. *Nature* **501**, 395–398 (2013).
- Nie, W. et al. Solar cells. High-efficiency solution-processed perovskite solar cells with millimeter-scale grains. *Science* **347**, 522–525 (2015).
- Stranks, S. D. et al. Electron-hole diffusion lengths exceeding 1 micrometer in an organometal trihalide perovskite absorber. *Science* **342**, 341–344 (2013).
- Kagan, C. R., Mitzi, D. B. & Dimitrakopoulos, C. D. Organic–inorganic hybrid materials as semiconducting channels in thin-film field-effect transistors. *Science* **286**, 945–947 (1999).
- Jeon, N. J. et al. Compositional engineering of perovskite materials for high-performance solar cells. *Nature* **517**, 476–480 (2015).
- Tan, Z. K. et al. Bright light-emitting diodes based on organometal halide perovskite. *Nat. Nanotechnol.* **9**, 687–692 (2014).
- Jeon, N. J. et al. A fluorene-terminated hole-transporting material for highly efficient and stable perovskite solar cells. *Nat. Energy* **3**, 682–689 (2018).
- Cao, Y. et al. Perovskite light-emitting diodes based on spontaneously formed submicrometre-scale structures. *Nature* **562**, 249–253 (2018).
- Menéndez-Proupin, E., Palacios, P., Wahnón, P. & Conesa, J. C. Self-consistent relativistic band structure of the CH₃NH₃PbI₃ perovskite. *Phys. Rev. B* **90**, 045207 (2014).
- Utzat, H. et al. Probing linewidths and biexciton quantum yields of single cesium lead halide nanocrystals in solution. *Nano Lett.* **17**, 6838–6846 (2017).
- Protesescu, L. et al. Nanocrystals of cesium lead halide perovskites (CsPbX₃, X = Cl, Br, and I): novel optoelectronic materials showing bright emission with wide color gamut. *Nano Lett.* **15**, 3692–3696 (2015).
- Li, J. et al. 2D Behaviors of excitons in cesium lead halide perovskite nanoplatelets. *J. Phys. Chem. Lett.* **8**, 1161–1168 (2017).
- Swarnkar, A. et al. Colloidal CsPbBr₃ perovskite nanocrystals: luminescence beyond traditional quantum dots. *Angew. Chem.* **54**, 15424–15428 (2015).
- Yarita, N., et al. Observation of positive and negative trions in organic–inorganic hybrid perovskite nanocrystals. *Phys. Rev. Mater.* **2**, 116003 (2018).
- Wang, Y., Zhi, M., Chang, Y. Q., Zhang, J. P. & Chan, Y. Stable, ultralow threshold amplified spontaneous emission from CsPbBr₃ nanoparticles exhibiting trion gain. *Nano Lett.* **18**, 4976–4984 (2018).
- You, Y. M. et al. Observation of biexcitons in monolayer WSe₂. *Nat. Phys.* **11**, 477–U138 (2015).
- Müller, M., Bounouar, S., Jöns, K. D., Glässl, M. & Michler, P. On-demand generation of indistinguishable polarization-entangled photon pairs. *Nat. Photon.* **8**, 224–228 (2014).
- Boyer, S. J. et al. Two-qubit conditional quantum-logic operation in a single self-assembled quantum dot. *Phys. Rev. B* **78**, 075301 (2008).
- Li, X. et al. An all-optical quantum gate in a semiconductor quantum dot. *Science* **301**, 809–811 (2003).
- Jayakumar, H. et al. Time-bin entangled photons from a quantum dot. *Nat. Commun.* **5**, 4251 (2014).
- Pan, J. W. et al. Multiphoton entanglement and interferometry. *Rev. Mod. Phys.* **84**, 777–838 (2012).
- Forbes, K. A., Ford, J. S. & Andrews, D. L. Nonlocalized generation of correlated photon pairs in degenerate down-conversion. *Phys. Rev. Lett.* **118**, 133602 (2017).
- Boyer, V., Marino, A. M., Pooser, R. C. & Lett, P. D. Entangled images from four-wave mixing. *Science* **321**, 544–547 (2008).
- Reischle, M., Beirne, G. J., Rossbach, R., Jetter, M. & Michler, P. Influence of the dark exciton state on the optical and quantum optical properties of single quantum dots. *Phys. Rev. Lett.* **101**, 146402 (2008).
- Bounouar, S. et al. Ultrafast room temperature single-photon source from nanowire-quantum dots. *Nano Lett.* **12**, 2977–2981 (2012).
- Grim, J. Q. et al. Continuous-wave biexciton lasing at room temperature using solution-processed quantum wells. *Nat. Nanotechnol.* **9**, 891–895 (2014).
- Castaneda, J. A. et al. Efficient biexciton interaction in perovskite quantum dots under weak and strong confinement. *ACS Nano* **10**, 8603–8609 (2016).
- Klimov, V. I. et al. Single-exciton optical gain in semiconductor nanocrystals. *Nature* **447**, 441–446 (2007).
- Hao, K. et al. Neutral and charged inter-valley biexcitons in monolayer MoSe₂. *Nat. Commun.* **8**, 15552 (2017).
- Lovering, D. J., Phillips, R. T., Denton, G. J. & Smith, G. W. Resonant generation of biexcitons in a GaAs quantum well. *Phys. Rev. Lett.* **68**, 1880–1883 (1992).
- Phach, V. D., Bivas, A., Hönerlage, B. & Grun, J. B. Biexciton resonant two-photon absorption in CuCl. *Phys. Status Solidi B* **84**, 731–740 (1977).
- Lodahl, P., Mahmoodian, S. & Stobbe, S. Interfacing single photons and single quantum dots with photonic nanostructures. *Rev. Mod. Phys.* **87**, 347–400 (2015).
- Halas, N. J., Lal, S., Chang, W. S., Link, S. & Nordlander, P. Plasmons in strongly coupled metallic nanostructures. *Chem. Rev.* **111**, 3913–3961 (2011).
- Day, J. K., Large, N., Nordlander, P. & Halas, N. J. Standing wave plasmon modes interact in an antenna-coupled nanowire. *Nano Lett.* **15**, 1324–1330 (2015).
- Russell, K. J., Liu, T. L., Cui, S. Y. & Hu, E. L. Large spontaneous emission enhancement in plasmonic nanocavities. *Nat. Photon.* **6**, 459–462 (2012).
- Lim, D. K. et al. Highly uniform and reproducible surface-enhanced Raman scattering from DNA-tailorable nanoparticles with 1-nm interior gap. *Nat. Nanotechnol.* **6**, 452–460 (2011).
- Kim, S. et al. High-harmonic generation by resonant plasmon field enhancement. *Nature* **453**, 757–760 (2008).
- Brongersma, M. L., Halas, N. J. & Nordlander, P. Plasmon-induced hot carrier science and technology. *Nat. Nanotechnol.* **10**, 25–34 (2015).
- Ji, B. et al. Non-blinking quantum dot with a plasmonic nanoshell resonator. *Nat. Nanotechnol.* **10**, 170–175 (2015).
- Park, Y. S., Guo, S., Makarov, N. S. & Klimov, V. I. Room temperature single-photon emission from individual Perovskite quantum dots. *ACS Nano* **9**, 10386–10393 (2015).
- Ridolfo, A., Di Stefano, O., Fina, N., Saija, R. & Savasta, S. Quantum plasmonics with quantum dot-metal nanoparticle molecules: influence of the Fano effect on photon statistics. *Phys. Rev. Lett.* **105**, 263601 (2010).
- LeBlanc, S. J., McClanahan, M. R., Jones, M. & Moyer, P. J. Enhancement of multiphoton emission from single CdSe quantum dots coupled to gold films. *Nano Lett.* **13**, 1662–1669 (2013).
- Takata, H. et al. Detailed observation of multiphoton emission enhancement from a single colloidal quantum dot using a silver-coated AFM tip. *Nano Lett.* **16**, 5770–5778 (2016).

44. Park, Y. S. et al. Super-Poissonian statistics of photon emission from single CdSe–CdS core–shell nanocrystals coupled to metal nanostructures. *Phys. Rev. Lett.* **110**, 117401 (2013).
45. Zhang, W., Govorov, A. O. & Bryant, G. W. Semiconductor–metal nanoparticle molecules: hybrid excitons and the nonlinear Fano effect. *Phys. Rev. Lett.* **97**, 146804 (2006).
46. Manjavacas, A., Garcia de Abajo, F. J. & Nordlander, P. Quantum plexcitonics: strongly interacting plasmons and excitons. *Nano Lett.* **11**, 2318–2323 (2011).
47. Miroshnichenko, A. E., Flach, S. & Kivshar, Y. S. Fano resonances in nanoscale structures. *Rev. Mod. Phys.* **82**, 2257–2298 (2010).
48. Zhang, Y. et al. Coherent anti-Stokes Raman scattering with single-molecule sensitivity using a plasmonic Fano resonance. *Nat. Commun.* **5**, 4424 (2014).
49. Zhang, W. & Govorov, A. O. Quantum theory of the nonlinear Fano effect in hybrid metal–semiconductor nanostructures: the case of strong nonlinearity. *Phys. Rev. B* **84**, 081405 (2011).
50. Chen, L. et al. Composition-dependent energy splitting between bright and dark excitons in lead halide Perovskite nanocrystals. *Nano Lett.* **18**, 2074–2080 (2018).
51. Becker, M. A. et al. Bright triplet excitons in caesium lead halide perovskites. *Nature* **553**, 189–193 (2018).
52. Sonnichsen, C. et al. Drastic reduction of plasmon damping in gold nanorods. *Phys. Rev. Lett.* **88**, 077402 (2002).
53. Becker, M. A. et al. Long exciton dephasing time and coherent phonon coupling in CsPbBr₂Cl Perovskite nanocrystals. *Nano Lett.* **18**, 7546–7551 (2018).
54. Lehmann, J. et al. Surface plasmon dynamics in silver nanoparticles studied by femtosecond time-resolved photoemission. *Phys. Rev. Lett.* **85**, 2921–2924 (2000).
55. Kaldun, A. et al. Observing the ultrafast buildup of a Fano resonance in the time domain. *Science* **354**, 738–741 (2016).
56. Song, J. et al. Quantum dot light-emitting diodes based on inorganic Perovskite cesium lead halides (CsPbX₃). *Adv. Mater.* **27**, 7162–7167 (2015).
57. Gourley, P. L. & Wolfe, J. P. Thermodynamics of excitonic molecules in silicon. *Phys. Rev. B* **20**, 3319–3327 (1979).
58. Phillips, R. T., Lovering, D. J., Denton, G. J. & Smith, G. W. Biexciton creation and recombination in a GaAs quantum well. *Phys. Rev. B* **45**, 4308–4311 (1992).
59. Bacher, G. et al. Biexciton versus exciton lifetime in a single semiconductor quantum dot. *Phys. Rev. Lett.* **83**, 4417–4420 (1999).
60. Lampert, M. A. Mobile and immobile effective-mass-particle complexes in nonmetallic solids. *Phys. Rev. Lett.* **1**, 450–453 (1958).
61. Kim, J. C., Wake, D. R. & Wolfe, J. P. Thermodynamics of biexcitons in a GaAs quantum well. *Phys. Rev. B* **50**, 15099–15107 (1994).
62. He, Y. M. et al. Cascaded emission of single photons from the biexciton in monolayered WSe₂. *Nat. Commun.* **7**, 13409 (2016).
63. Zhang, Y. et al. Sub-nanometre control of the coherent interaction between a single molecule and a plasmonic nanocavity. *Nat. Commun.* **8**, 15225 (2017).
64. Südmeyer, T. et al. Femtosecond laser oscillators for high-field science. *Nat. Photon.* **2**, 599 (2008).
65. Klimov, V. I. Mechanisms for photogeneration and recombination of multiexcitons in semiconductor nanocrystals: implications for lasing and solar energy conversion. *J. Phys. Chem. B* **110**, 16827–16845 (2006).
66. Pedersen, T. G., Pedersen, K., Cornean, H. D. & Duclos, P. Stability and signatures of biexcitons in carbon nanotubes. *Nano Lett.* **5**, 291–294 (2005).
67. Wu, X., Gray, S. K. & Pelton, M. Quantum-dot-induced transparency in a nanoscale plasmonic resonator. *Opt. Express* **18**, 23633–23645 (2010).
68. Sapori, D., Kepenekian, M., Pedesseau, L., Katan, C. & Even, J. Quantum confinement and dielectric profiles of colloidal nanoplatelets of halide inorganic and hybrid organic-inorganic perovskites. *Nanoscale* **8**, 6369–6378 (2016).

Acknowledgements

The authors thank the support from the Ministry of Science and Technology (2017YFA0205700, 2017YFA0304600, 2016YFA0200700 and 2017YFA0205004), National Natural Science Foundation of China (Nos. 21673054, 11874130, 61774003, 61521004), Beijing Municipal Natural Science Foundation (4182076 and 4184109). Q.Z. acknowledges the support of start-up funding from Peking University, one-thousand talent programs from Chinese government, open research fund program of the state key laboratory of low-dimensional quantum physics.

Author contributions

X.L., Q.Z. conceived the idea for the manuscript and designed the experiments. J.C., W.D., Y.M., Q.S., J.S., S.Z., X.S., X.W. and R.W. conducted the spectroscopic characterization. B.P. and H.Z. and P.L. prepared the perovskite QDs. J.C., W.D. fabricated devices and performed TEM, SEM, and AFM. J.C. performed the simulations. X.L., Q.Z., T.C.S., X.Q. and G.X. contributed to the data analysis. All the authors discuss the results and the manuscript. Q.Z. and X.L. led the project.

Additional information

Supplementary information accompanies this paper at <https://doi.org/10.1038/s42005-019-0178-9>.

Competing interests: The authors declare no competing interests.

Reprints and permission information is available online at <http://npg.nature.com/reprintsandpermissions/>

Publisher's note: Springer Nature remains neutral with regard to jurisdictional claims in published maps and institutional affiliations.



Open Access This article is licensed under a Creative Commons Attribution 4.0 International License, which permits use, sharing, adaptation, distribution and reproduction in any medium or format, as long as you give appropriate credit to the original author(s) and the source, provide a link to the Creative Commons license, and indicate if changes were made. The images or other third party material in this article are included in the article's Creative Commons license, unless indicated otherwise in a credit line to the material. If material is not included in the article's Creative Commons license and your intended use is not permitted by statutory regulation or exceeds the permitted use, you will need to obtain permission directly from the copyright holder. To view a copy of this license, visit <http://creativecommons.org/licenses/by/4.0/>.

© The Author(s) 2019